Renewable Energy 205 (2023) 222–237

Contents lists available at ScienceDirect

Renewable Energy

journal homepage: www.elsevier.com/locate/renene

Using internal sinusoidal fins and phase change material for performance enhancement of thermal energy storage systems: Heat transfer and entropy generation analyses

Ali Tavakoli [a], Mahmood Farzaneh-Gord [a,*], Amir Ebrahimi-Moghadam [b]

[a] Mechanical Engineering Department, Faculty of Engineering, Ferdowsi University of Mashhad, Mashhad, Iran
[b] Mechanical Engineering Department, Faculty of Engineering, Quchan University of Technology, Quchan, Iran

ARTICLE INFO

Keywords:
Phase change material (PCM)
Thermal energy storage (TES)
Sinusoidal fin
Heat transfer
Entropy generation

ABSTRACT

In comparison to sensible energy storage, LHTES (Latent Heat Thermal Energy Storage) offers large storage energy densities per unit mass/volume at nearly constant temperatures. This study is carried out to assess thermo-hydraulic performance of the simultaneous utilization of sinusoidal internal fins and PCM (Phase Change Material) in LHTES systems. For this, a validated numerical framework is developed using Ansys-Fluent software. The RT82 is considered as working substance in a transient laminar flow. The geometrical parameters of fins, (including length, height, and thickness) are evaluated by defining 15 different geometries to look for the most optimal case in terms of faster PCM melting. Furthermore, the impact of fins' material (copper and gold) is also involved in the investigations. A comprehensive sensitivity analysis is conducted to completely investigate different heat transfer and thermodynamic characteristics. The results illustrated that in case 4 (with H/L = 0.125 and thickness of 3 mm), the highest growth of normalized liquid fraction compared to normalized heat transfer coefficient is achieved which results in Dhl number of about 0.55. Also, the second-law analysis revealed that the lowest entropy is generated in this case. So that, 62% increment of liquid fraction and 59.5% reduction of entropy generation is observed in case 4 compared to a case with simple straight fins.

1. Introduction

Phase Change Material (PCM) is one of the most key and important parts of a thermal and energy system such as solar collectors, heat exchangers, batteries and especially in a LHTES (Latent Heat Thermal Energy Storage) system [1–6]. In LHTESs, the used PCM must have some characteristics to increase the energy storage density and deliver thermal stability under long-term cycling. Relying on the previous investigations, some of the main characteristics of PCMs are presented as a graphical sketch in Fig. 1 [7,8]. These properties are included thermal, physical, and chemical characteristics, and some economic factors which should be taken into account to select a proper PCM in an LHTES system (Zhang et al. [9]). There is also a very strong relationship between performance of a storage system and characteristics of the PCM. As another new aspect in a storage system, utilizing fins with different shapes has attracted the attention of many researchers. These fins are extended surfaces [10] that are utilized for the increment of conductive heat transfer rate.

Several investigations have been numerically conducted through CFD simulations on the melting process of PCM with various fins [11–13]. There are various works done by several researchers on PCMs for different applications. Pizzolato et al. [14] utilized CFD (Computational Fluid Dynamic) approach and topological optimization to design high-conductive fins for fast PCM melting and solidification in shell-and-tube LHTES. The researchers concluded that this configuration reduces the charging time required to reach 95% of the storage capacity by 27%, and the discharge time by 11%. They also reported that topological optimized design leads to expedition of 37% and 15% in charging and discharging processes, respectively. Sheikholeslami et al. [15] utilized nanoparticle-enhanced PCM and fins for improving the heat transfer efficiency of a LHTES. For this, he developed a transient CFD model and reached to optimum nanoparticle diameter of 40 nm. Yagci et al. [16] assessed thermal behavior of a PCM in a tube-in-shell LHTES system. They also embedded rectangular fin inside the system and evaluated the impact of its edge length ratio. They stated inserting fins results in 52% reduction of the melting compared simple case. Dai et al.

* Corresponding author.
E-mail address: m.farzanehgord@um.ac.ir (M. Farzaneh-Gord).

https://doi.org/10.1016/j.renene.2023.01.074
Received 23 October 2022; Received in revised form 22 December 2022; Accepted 19 January 2023
Available online 22 January 2023

[17] considered the water as a PCM in a horizontal tube LHTES and placed simple straight fins inside it. They derived a computational model to assess thermal behavior and charging time. Their findings proved that fins' position has a significant effect and reached up to 40% efficiency enhancement using by the best fin configuration. Gürtürk and Kok [18] experimentally and numerically investigated the effects of fins on PCM melting. They suggested some specific types of fins for the improvement of the melting process of PCM in non-melted regions of thermal storage systems. Kok [19] also accomplished an experimental work for investigating the effects of nanoparticles and fins on the energy storage efficiency of PCM. His observations revealed that utilization fins can shorten the melting time by 63%. In another published work, the application of a PCM on exterior walls of a residential building was evaluated by Pirasaci [20]. The purpose of the study was focused on the examination of how heating and cooling differ in different seasons (the city of Ankara was assumed as a case study). Results demonstrated that the PCM layer integration reduces the winter season's heating energy demand. Arici et al. [21] utilized ANSYS Fluent software to evaluate the melting performance of PCM by nanoparticles and interior fins. They stated that simultaneous utilization of nano-enhanced PCM leads 54% increment of melting rate. Yang et al. [22] utilized a double PCM of lauryl alcohol and stearic acid in a suitable thermal environment with nanoparticles (LA-SA/Al2SO3) for heating and cooling application. They showed that Al2SO3 nanoparticles with a volume fraction of 0.5% can improve the LA-SA nanoparticles thermal conductivity by 43%. Li et al. [23] developed a CFD framework to assess the effects of dispersing nanoparticle additives together with embedding straight internal fins in the process of solidification. They stated that the solidification process velocity is directly related to the length of fins and platelet shape for nanomaterials. Zhao et al. [24] also don a study on the arrangement of fins and meta foam effects on PCM. Their results illustrated, in the case of choosing the optimal number of fins, the melting time declines by 60%. A study on the enhancement of the solidification of PCM through finned pipes was done by Santos et al. [25] They investigated the impact of some parameters (including fin diameter, wall temperature, and mass flow rate) and developed some new correlations for predicting melting interfaces. A Numerical analysis was carried out by Taghilou and Khavasi [26] to study the thermal characteristic of a heat sink filled with PCM. Their results illustrated that the increment of heat flux at lower and higher heat fluxes increases and decreases the heat transfer coefficient, respectively. Xu et al. [27] embedded C58, a PCM based on sodium acetate trihydrate, in a LHTES system based on shell-and-tube heat exchanger. They conducted experimental tests for two modes of T-history and full-scale and evaluated thermal behavior of PCM. Nakhchi et al. [28] developed a CFD model to study the effects of nanoparticles and stair fins geometry on the performance improvement of PCM LHTES. The highest energy storage capacity was obtained as 474.1 kJ by using stair fins with stair ratio of 4 at volume concentration of 1.5%. For the investigation of the storage performance of LHTES. Soltani et al. [29] studied efficiency improvement of a tube LHTES by utilizing three methods including: addition of Cu nanoparticles into *N*-eicosane PCM, inserting simple straight fins, and rotating the tube. They observed 74% and 70% reduction of melting and solidification time using by the optimal case compared to the base one. Zheng et al. [30] combined the GA (Genetic Algorithm) optimization and CFD approaches Y- and arrow-shaped fins inside a LHTES system. They sought the minimum distance between fins and PCM as the optimization target. Comparing the outputs of these two models, the arrow-shaped fins showed 52.8% less solidification time.

Other research categories in this field include photovoltaic thermal (PVT), thermoelectricgenerators (TE), thermal control units, and solar stills. In recent years, PCMs have received considerable attention due to their significance in the renewable energy sector, particularly in solar-powered buildings and solar-powered plants. In one recently published paper in this category, Li et al. [31] developed a CFD framework and applied energetic and exergetic analyses to assess the melting performance of using PCM and twisted fins in a LHTES utilized in a solar farm. They found that triple and double fins respectively have the highest efficiency in vertical and horizontal orientations. Yousef and Hassan [32] derived eco-exergy and environmental models to assess the feasibility of using PCM in a solar still. Their experiments illustrated that the utilization of PCM with low phase change temperature is more feasible in regions with low radiation intensity. In another work, PCMs were experimentally applied to a conventional flat plate solar collector by Palacio et al. [33]. Two different PCMs and solar collectors with different inclination angles were used in this analysis. Thermal

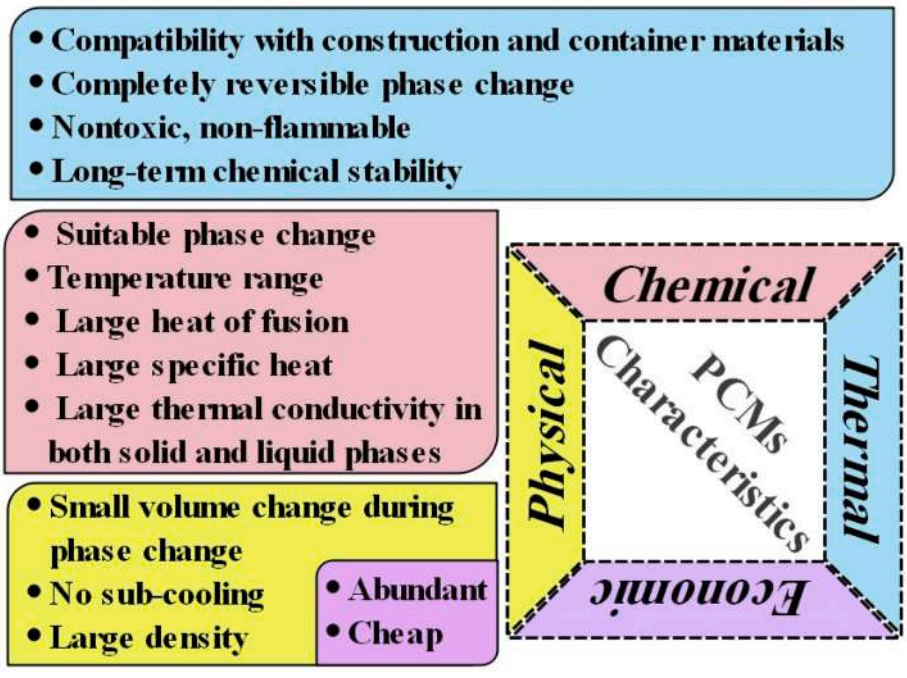

Fig. 1. Some key characteristics of PCMs.

efficiency can be increased from 26% to 28% in the mentioned cases. Vigneswaran et al. [34] conducted a thermal performance study for three different passive solar stills with 0, 1, or 2 PCMs. Compared to the passive still without PCM, the use of one or two PCM results in daily efficiency increment of 3.57% and 7.57%, respectively. The wide range of applications and many applications of PCMs in industries prompted some scholars to focus on their use in heat exchangers. Mahdi et al. [35] investigated the effect of some design parameters in PCM melting processes for double-pipe helical-coil-tube and shell-and-tube heat exchangers. Sathe and Dhoble [36] simulated the RT42 PCM inside a rectangular enclosure LHTES fitted with external fines with an application in solar PV systems. Their analyses showed that at inclination angle of 30° the Nusselt number is increased by 6–9 times. Another unsteady numerical simulation was carried out by Sarani et al. [37] to study the effects of fins and nanoparticles on the solidification and energy storage of PCM. In comparison to continuous copper and aluminum fins, discontinuous fins can reduce energy release time by 90% and 85%, respectively. Nakhchi and Esfahani [38] installed stepped fins to improve PCM LHTES systems efficiency. They applied CFD approach for their analysis and suggested that stepped fins have a faster process of melting than the horizontal typical fins. Duan et al. [39] showed that installing PCM in the south wall is the best option, cutting energy use by 30%. However, with passive thermal release, the integrated PCM solar wall cannot entirely release heat at night. Kabeel et al. [40] designed a modified version of a solar still comprising an absorber v-shaped corrugations and PCM. They experimentally tested this proposal and compared it with its basic configuration. They reached to 0.0026 $ cost saving in producing each liter of fresh water with the modified case. Also, Hou et al. [41] used numerical analysis to examine the flow and heat transfer properties of a phase shift with two-dimensional rotation of the three-dimensional rectangular encapsulated container (PCM-REC) filled with paraffin (RT -27). Moreover, the majority of phase transition materials used in latent heat thermal energy storage have weak thermal conductivity in both the liquid and solid phases, which results in ineffective heat transmission. Pu et al. [42] applied multiple utilization of PCMs and gradient copper foam to increase the effectiveness of heat transfer and speed up the melting of PCMs in order to get around this restriction. Selimefendigil et al. [43] combined the use of a magnetic field with a wavy conductive wall during hybrid nanoliquid convection to propose a novel way of managing the phase transition dynamics in a PCM-installed container. Reynolds number (Re: 100–500), magnetic field strength (Ha: 0–30), amplitude (Af: 0–0.2), wave number (Nf: 2–16) of the wavy partition, and conductivity ratio were all varied in their work (Kr: 0.1–50).

From the above literature review it could be concluded that there are many numerical and experimental researches around two efficiency improver methods of LHTES systems: utilizing PCMs and internal fins. But to the best of authors' knowledge, very limited researches have been conducted simultaneous use of these two methods in LHTES systems. Furthermore, the limited published works utilized fins with specific shapes and only studied the heat transfer characteristics of the problem. Hence, another gap is the lack of investigation which paid to study both of the heat transfer and entropy generation analyses. These motivate us to propose a novel shape fin and use PCM in a LHTES system which results in the increment of thermal energy storage performance and accelerated melting. For bridging the mentioned deficiencies in the available literature, as the first study in the field, the effects of utilizing sinusoidal fins and PCM on the heat transfer characteristics and entropy generation within a LHTES system are going to be assessed in the current study. For this, a robust and validated CFD model is developed.

2. Numerical model and formulation

The objective of this section is focused on discussing the problem under investigation, the geometry and PCM characteristics, as well as the governing equations. All of these items are described in detail below.

2.1. Physical model description and grid generation

The studied device is a LHTES with PCM which can be used in a solar still system (Fig. 2a). Due to its high energy storage density and isothermal operation, the adoption of PCMs in a solar home hot water system would enhance the system's performance. Tanks used for energy storage benefit from phase transition materials' improved thermal stratification [44]. The schematic view of the enclosure of the LHTES with sinusoidal fins is depicted in Fig. 2b. The sinusoidal fin is utilized due to its superiority in heat transfer and lower entropy generation over other fin shapes [45]. The enclosure's height (l) is kept constant at 120 mm, while its width (D) is at 50 mm. Also, various fins with different geometrical parameters are sought. So that, the effects of length, height, and thickness are investigated on the heat transfer and entropy generation. Furthermore, the impact of fins' materials is also investigated (copper and gold fins are sought). For this, as there are a large number of cases with different geometries, some specific cases are defined in Table 1 and the results are gone to be presented for these cases. Furthermore, three various numbers of fins with different direction and area are used in the simulations. Taking into consideration the shape of fins and LHTES, unstructured mesh is utilized in this investigation (a sample of the generated grid is depicted in Fig. 3). Finally, it is worth noting that the RT82 is chosen as the PCM due to its high latent heat capacity and chemical stability [46]. Table 2 lists the thermo-physical parameters of the chosen materials in greater detail.

2.2. Governing equations and boundary conditions

In this paper, a two-dimensional (2D) transient laminar flow of RT82 (as PCM) inside a LHTES with sinusoidal fins is modeled. The following assumptions are made for the governing equation of the proposed PCM technique inside the TTHX's center tube [48].

- During melting, natural convection is considered using the Boussinesq approximation, which is valid for density variations and buoyancy forces. Otherwise, they are ignored.
- The thermophysical exclusivity of the HTF and PCMs is not dependent on the presence of heat; the necessary conditions based on the earlier presumptions, including mass, momentum, and energy preservation, are as follows:

$$\nabla.\vec{V}=0 \tag{1}$$

$$\frac{\partial\vec{V}}{\partial t}+\vec{V}.\nabla.\vec{V}=-\frac{1}{\rho}\nabla P+\frac{\mu}{\rho}\nabla^2\vec{V}+\beta g\left(T-T_{\mathrm{ref}}\right)+A_{\mathrm{mush}}\vec{V}\frac{(1-\lambda)^2}{\lambda^3+\varepsilon} \tag{2}$$

$$\frac{\partial}{\partial t}(\rho h_e)+\nabla\left(\rho\vec{V}h_e\right)=\nabla(k\nabla T) \tag{3}$$

where, the parameters of $\vec{V}$, P, ρ, μ, and β stand for the velocity, pressure, density, dynamic viscosity, and thermal expansion coefficient. Darcy's law damping is represented by the right-hand side term at the end of Eq. (3). In this study, A_{mush} is set to 10^6, which is commonly the value of the mushy zone constant. The denominator also contains a small number ($\varepsilon=0.001$) to anticipate the division by zero [49]. Also, λ is the fluid fraction characterized concurring to the temperature varieties in each computational cell, and H is enthalpy, which these two parameters are respectively defined as Eqs. (4) and (5):

$$\lambda=\begin{cases}0 & if\ T<T_s\\ \dfrac{T-T_s}{T_l-T_s} & if\ T_s<T<T_l\\ 1 & if\ T>T_l\end{cases} \tag{4}$$

The enthalpy h_e is defined as follows:

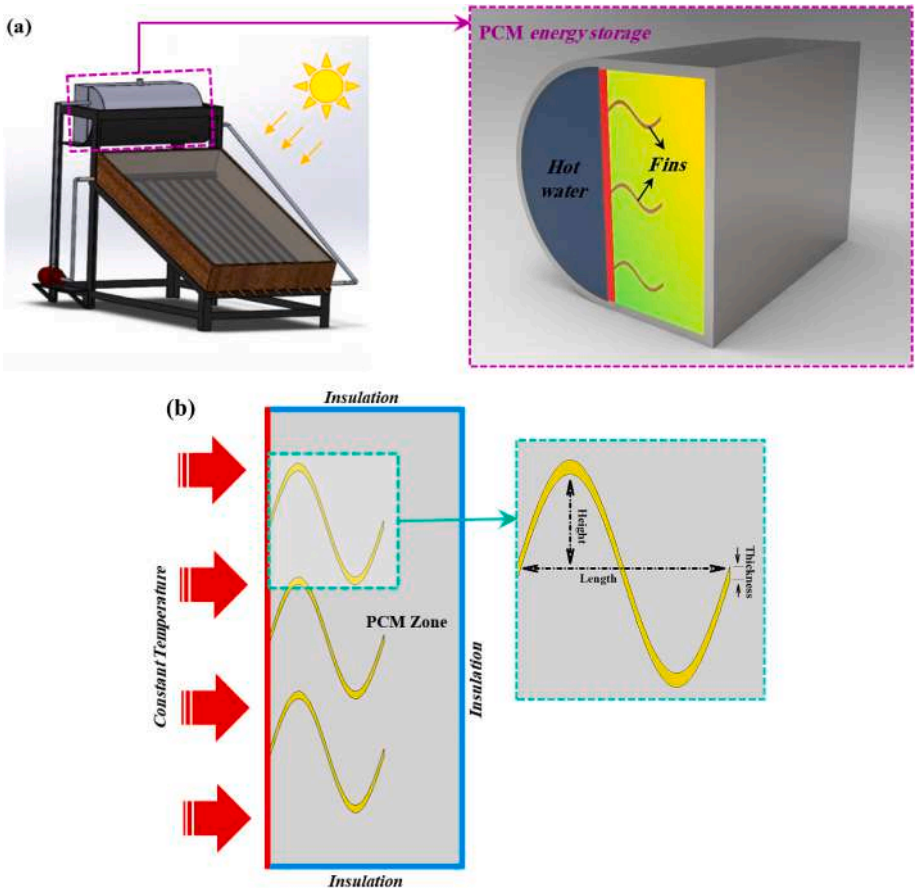

Fig. 2. A schematic portrait of the, (a) application of the studied device, (b) LHTES geometry with sinusoidal fins.

Table 1
Geometrical parameters of the defined cases.

Case no.	Length (mm)	Height (mm)	Thickness (mm)	H/L (−)
Simple straight	20	0	2	0
Case 1	30	15	2	0.5
Case 2	30	10	2	0.333
Case 3	20	10	2	0.5
Case 4	40	5	3	0.125
Case 5	20	5	1	0.25
Case 6	30	10	3	0.333
Case 7	40	5	1	0.125
Case 8	40	10	2	0.25
Case 9	20	5	3	0.25
Case 10	20	15	1	0.75
Case 11	20	15	3	0.75
Case 12	40	15	3	0.375
Case 13	30	10	1	0.333
Case 14	30	5	2	0.166
Case 15	40	15	1	0.375

$$h_e = \left(h_{\text{ref}} + \int_{T_{\text{ref}}}^{T} C_P dT \right) + \lambda \Gamma \tag{5}$$

in which, h_{ref}, Γ, and C_P indicate the reference enthalpy at the reference temperature of T_{ref}, respective heat capacity, and fusion idle heat.

After deriving the CFD governing equations, assumptions related to the numerical solution procedure and appropriate boundary conditions should be taken into consideration. The left wall in the current investigation is heated isothermally at 363.15 K, while the other three walls are insulated. The PCM starts at a temperature of 300.15 K. Also, general assumptions of the solver and boundary conditions are tabulated in Table 3.

The main output of the above procedure is the determination of velocity and temperature within the calculation domain. As the final step, the heat transfer and entropy generation formula are derived in this section. The following equations can be used to calculate heat transfer coefficient (h) and Nusselt number (Nu) [50,51]:

$$h = \frac{Q}{T_{\text{wall}} - T_{\text{bulk}}} \tag{6}$$

$$\text{Nu} = \frac{hD_H}{k} \tag{7}$$

As another heat transfer index, the Stefan number (Ste) is considered to be investigated in this study. This dimensionless number is defined as the ratio of sensible and latent heat terms. The temperature difference between two phases is a constant value. As transient problem is simulated in this study, to investigate this parameter during the time, a modified version of Ste number is defined as momentary Ste number (Eq. (8)). Here, the surface temperature T directly affects the value of the Stefan number and is defined as:

$$\text{Ste}_{\text{mom}} = \frac{c_{P,l} \overbrace{\Delta T_{\text{PCM}}}^{T - T_{\text{mom}}}}{H_L} \tag{8}$$

where, c_{Pl} is the specific heat of the liquid PCM in the melting process, H_L is the latent heat of PCM in melting, and T_{mom} is the momentary temperature of PCM.

In the next step, the entropy generation analysis formula are derived. The entropy generation describes the system's irreversibility sources, which include viscous and thermal irreversibilities. These two terms are respectively due to the fluid flowing inside the system and heat transfer.

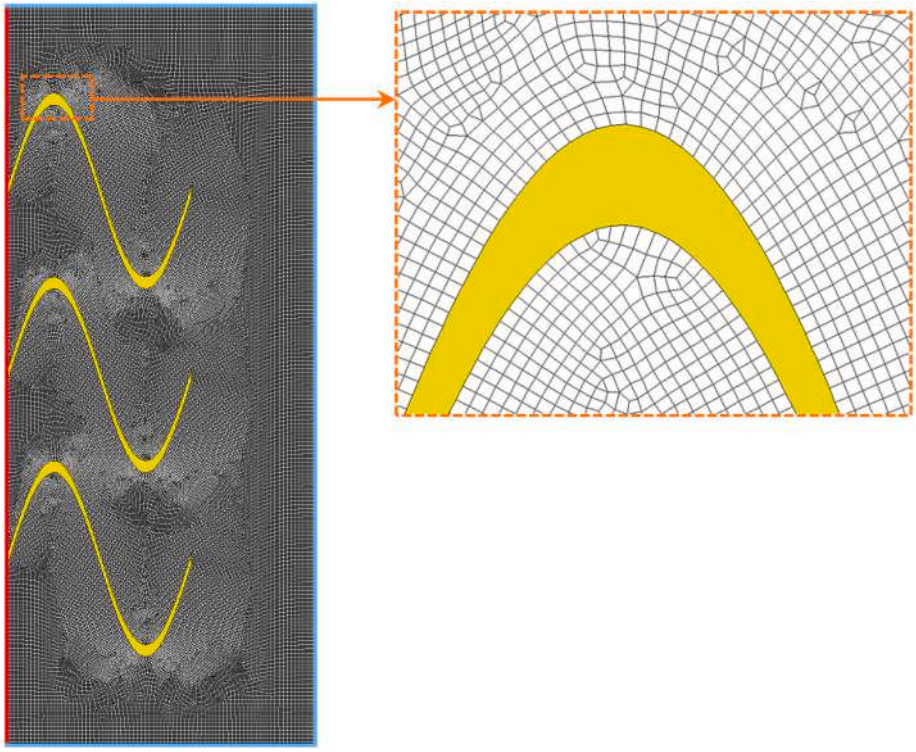

Fig. 3. The generated mesh within the LHTES and around fins.

Table 2
Thermo-physical parameters of the considered PCM [47].

Item	Value
Name	RUBITHERM 82
Density, solid, ρ_s (kg/l)	0.95
Density, liquid, ρ_l (kg/l)	0.77
Specific heat, liquid $C_{P,l}$ (J/g.K)	2
Latent heat of fusion, H_L (J/g)	176
Melting temperature, T_m (C)	77–82
Thermal conductivity, k (W/m.K)	0.2
Thermal expansion coefficient, β (1/K)	0.001
Dynamic Viscosity, μ (kg/m.s)	0.03499

Table 3
General solver parameters and boundary conditions.

Item	Description
CFD solver program	Fluent v. 21.0.0, 2D, Double precision
Solver assumptions	Pressure-based, Absolute velocity, and Transient
Viscous model	Laminar
Materials	PCM: RUBITHERM 82
	Fins: Copper and Gold
Boundary conditions	Left wall: Constant temperature
	Right, top, and bottom walls: Insulation
	No-slip wall for solids

So that, the entropy generation can be considered as a comprehensive thermo-hydraulic variable. Because it consists both of the frictional (fluid flow) and thermal (heat transfer) phenomenon. Summing frictional and thermal entropies produces the total volumetric entropy generation rate (Eq. (9) [52]). The generation rates of local frictional and thermal entropy are calculated using Eqs. (10) and (11) for a Cartesian coordinate system (x, y) [53,54].:

$$\dot{S}'''_{g,\mathrm{tot}} = \dot{S}'''_{g,f} + \dot{S}'''_{g,h} \tag{9}$$

$$\dot{S}'''_{g,f} = \frac{\mu}{T}\left\{2\left[\left(\frac{dv_x}{dx}\right)^2 + \left(\frac{dv_y}{dy}\right)^2\right] + \left(\frac{dv_x}{dy} + \frac{dv_y}{dx}\right)^2\right\} \tag{10}$$

$$\dot{S}'''_{g,h} = \frac{k}{T^2}\left[\left(\frac{dT}{dx}\right)^2 + \left(\frac{dT}{dy}\right)^2\right] \tag{11}$$

Any point in the computational domain is calculated for local entropy generation. To calculate the entropy production, the distribution of entropy generation will be integrated over the total volume. Total entropy is calculated using the following equations [55]:

$$\dot{S}_{g,h} = \int \dot{S}'''_{g,h}\mathrm{d}V \;;\; \dot{S}_{g,f} = \int \dot{S}'''_{g,\mathrm{f}}\mathrm{d}V \;;\; \dot{S}_{g,\mathrm{tot}} = \int \dot{S}'''_{g,\mathrm{t}}\mathrm{d}V \tag{12}$$

In the above equations, the parameters of $\dot{S}'''_g$ and $\dot{S}_g$ show volumetric entropy generation rate and entropy generation rate, respectively. Also, the subscripts of f, h, and tot refers to the frictional, thermal, and total parts of entropy generation.

3. Model validation

In order to validate the present numerical simulation, the results are compared with the experimental data of Al-Abidi et al. [46]. Fig. 4 shows a comparison between the current numerical results and experimental data of the reference study for the average melting temperature. There is a good agreement between numerical results and experimental data in this comparison. 2.8% is the maximum relative deviation.

The small differences between the results could be attributed to the study's assumptions, which included holding the PCM characteristics and volume steady, using 2D modeling, accounting for heat loss to the environment, and taking into account the instability of the measurement equipment during the tests.

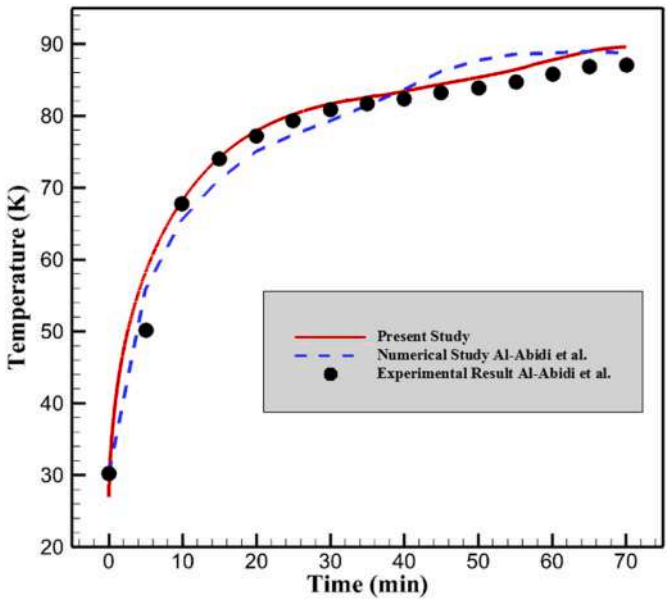

Fig. 4. Al-Abidi et al. experimental data and the current numerical simulation [46].

4. Grid and time-step independent study

The grid independence analysis conducted in this study to identify an acceptable number of elements is shown in Fig. 5. Due to the good agreement of the data obtained from the two sizes of medium and fine grid, the medium size for similar thighs can be used to reduce the computational cost. After the grid study, the independence of the time-step is examined. The results of the time-step independence test for the number of 34,000 elements are shown in Fig. 6. According to the results, the appropriate time-step is 1 s. Besides, taking into account the three time-steps in autonomy test and step size of 0.5, 1, and 2 s are conducted with a fixed grid number of 34,000 cells, as presented in Fig. 6. After their comparison, it appeared that the most extreme deviation between time-steps of 0.5 and 1 s is 0.003%. Concerning over decreasing computational time and high precision, this study selected the time step of 1 s for advanced simulation.

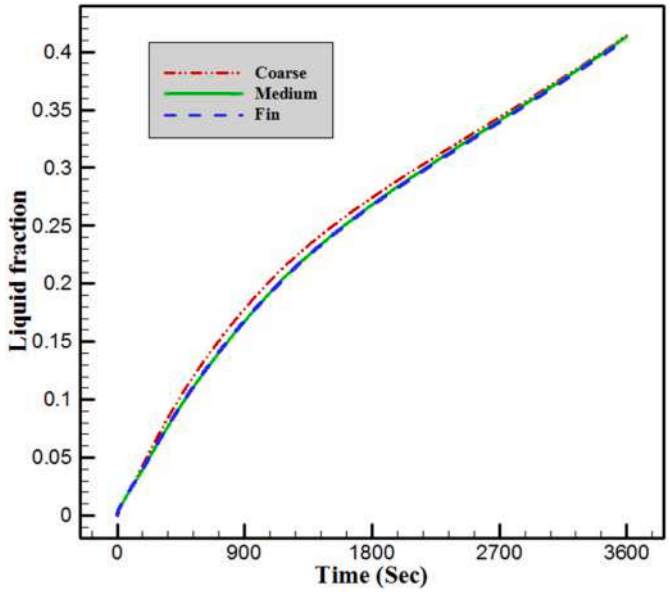

Fig. 5. Independence study of grid size in terms of liquid fraction versus time in a time-step equal to 1 s.

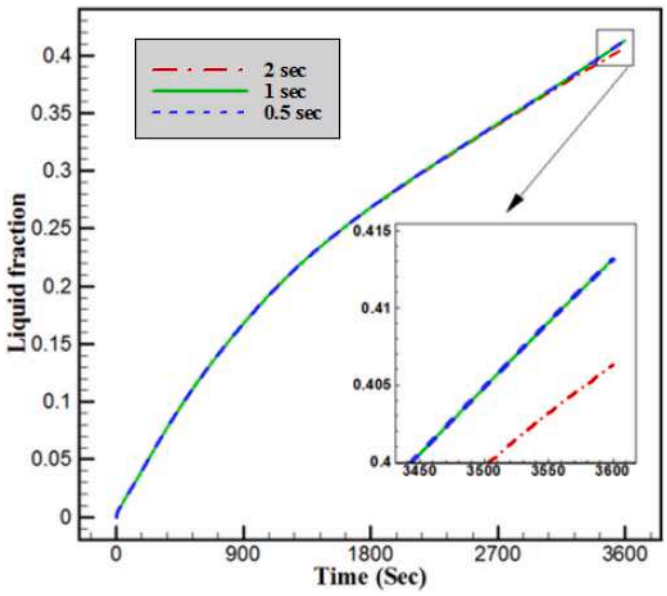

Fig. 6. The outputs of time-step independency investigation for the liquid fraction variable across time, in the 34,000 number of elements.

5. Results and discussion

In this section, the outputs of the simulation are comprehensively presented. Firstly, a comprehensive sensitivity analysis is conducted to know the influence of the fins' material and direction. This process is done for a sample case and the melting fraction is shown in Fig. 7. Here, two materials of copper and gold are assessed and this figure proves that gold can be a more suitable choice because of it leads to higher melting liquid fraction. But due to the high cost of gold compared to copper, we used copper in modeling, all the results are presented for copper.

In the next procedure, four different possible directions for arrangement of fins are sought and those melting fraction is presented in Fig. 8. In this figure, as it turns out, the –Y direction is the best choice followed by –X, +X, and +Y directions. The reason is behind in the achievement of higher liquid fraction on –Y direction than the rest of the directions.

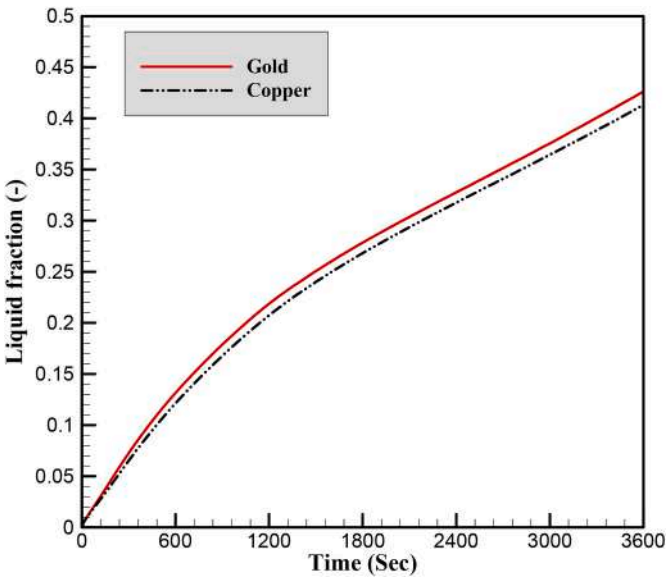

Fig. 7. Comparison between the liquid fraction of the gold and copper fins for the case 5.

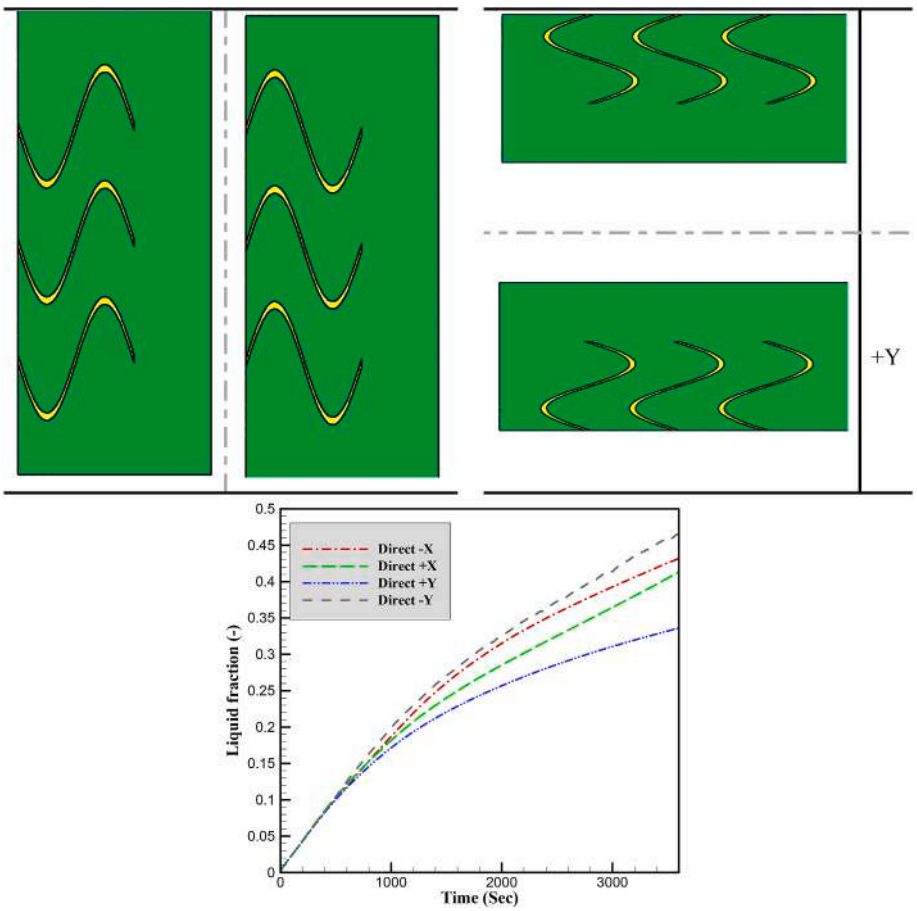

Fig. 8. Comparison between the liquid fraction of different fins direction for case 9.

Due to the heated fins, -Y displays a higher liquid percentage. The liquid percentage around -Y fins is significantly higher than that of +Y, -X, and +X fins, which have natural convection and lower density fluid, because of the trapped zone of heat at the bottom of those fins.

Heat tends to travel upward between the -Y fins due to natural convection, which causes heat retention. Heat will be trapped between the fin walls and the enclosure walls with -Y fins, though. However, since the sinusoidal fins eliminate the vertical obstruction, -Y fins enable the heat to flow more readily.

Fig. 9 shows the effect of different fin geometries on the liquid fraction and number for different H/L ratios during time spending. This figure shows that for different lengths, thicknesses, and heights, the PCM starts melting at the bottom and left corners, then spreads to the middle section, and finally shifts to the top left corner to complete the melting process. Due to the increase in natural convection flow with these fin geometries, there is no significant difference between the fins at initial time-steps (t = 1800 s). As a result of the heated fins, the density decreases, forcing the flow. As a matter of fact, in the case of a same length and height, the melting time for fins with higher thicknesses is shorter than for fins with smaller thicknesses. A more uniform temperature distribution within the enclosure is the main reason for the lower melting time for sinusoidal fins with higher thickness. Natural convection accelerates the melting process on the upper side, and the thickest fins on the lower side can intensify the melting process. As shown in Fig. 9, the H/L ratio has an effect on the H/L ratio. The melting process is fast at the beginning of the melting process for both the highest and lowest thicknesses (i.e. H/L = 0.125 in cases of 4 and 7), but slows with increasing melting time (t = 3600 s). There are two main reasons for this phenomenon. As the H/L increases, the heated surface increases, and as a result, more heat is transferred to PCM, causing melting to occur more quickly. Due to natural convection, lower H/L ratios make a region between the fins where fluid is trapped. As the melting process begins (at t = 1800 s), this region contributes to more heat transfer and therefore a faster melting process. Heat is transferred from the heater plate to the PCM at a rate characterized by the *Nu* number. At the beginning of the process, all cases exhibit a high number value. The thermal resistance to heat transfer from the heater surface to the solid PCM is initially very low since there is only a thin layer of liquid PCM on top of the heater surface. However, as the liquid layer grows, the thermal resistance increases and the number considerably drops. In a PCM system without fins, the value of the number decreases almost to zero at the conclusion of the melting process, but it doesn't change in a finned PCM system. Fig. 9 shows *Nu* number enhancement with finned-based systems. With the finned-based PCM system, the Nusselt number is greatly improved during the final phase of melting. All PCM systems with fins show, on average, 3–5 times improvement over their comparable no-finned counterparts. The enhancement brought about by an increase in the Nusselt number of fins is greater in larger PCM thickness configurations than in smaller PCM thickness configurations.

The liquid fraction distribution for different fin geometries is plotted in Fig. 10 for two time steps. In this figure, depending on the thickness, all the defined cases are classified into three categories and the contour plot of each category is presented for different lengths and heights. As can inferred, the fins' length is more effective parameter than the height. For example, the only difference in cases of 9 and 11 is in their height; in the beginning, case 11 melts better, but after a while, Case 9 surpasses it. So that the contour of case 11 has more liquid fraction than case 9 before 30 min; but at 60 min, the figure illustrates that case 9 contains more liquid fraction. This phenomenon can also be demonstrated based on Fig. 9 and as can be seen, in 2900 s, the curves of cases 9 and 11 intersected and after this time, case 9 produced more liquid fraction, which can be said that the growth rate of liquid fraction decreased after

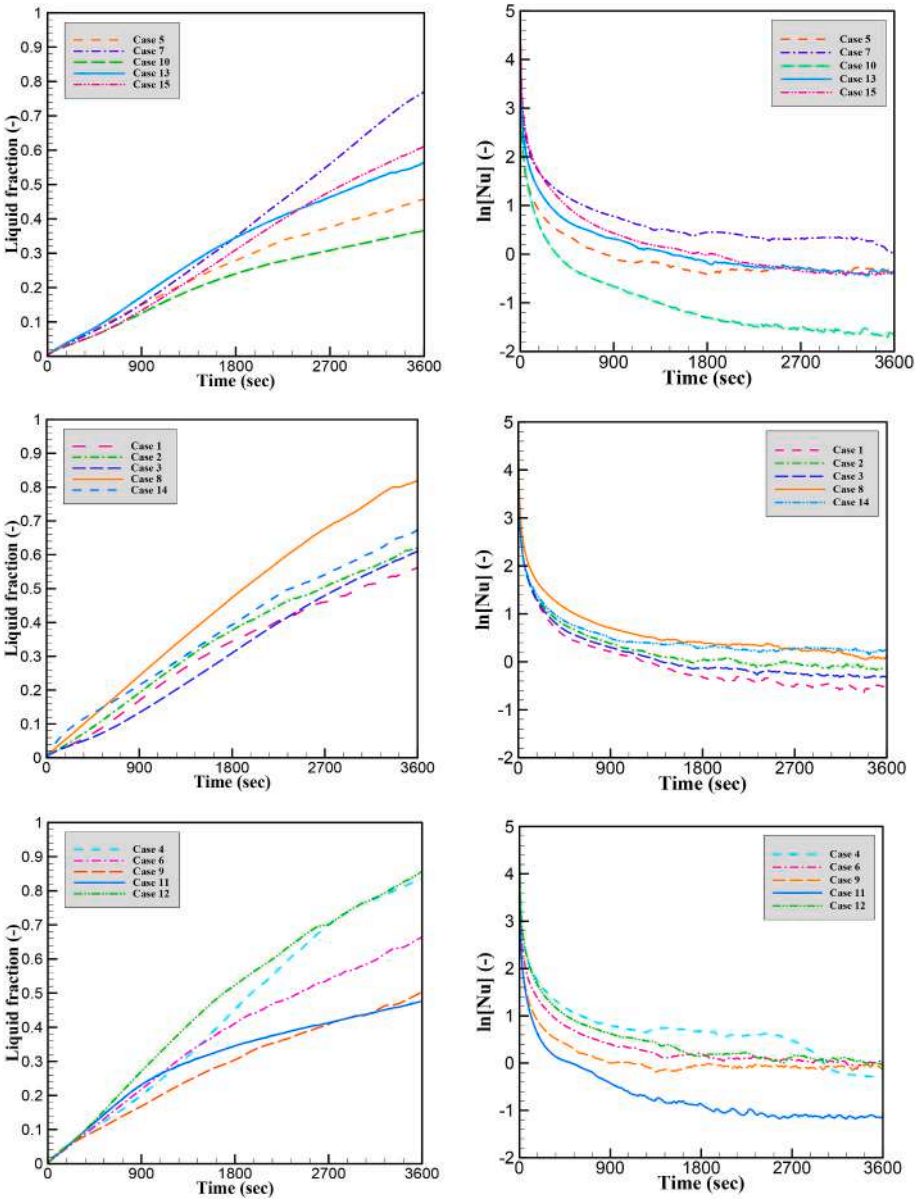

Fig. 9. Variation of the liquid fraction and Nusselt number versus time for different defined cases.

this period of time. The same trend has occurred for cases of 4 and 12, but this issue has not affected the rest of the thicknesses, which shows that the thickness is a significant factor in how this phenomenon occurred. Finally, relying on Figs. 9 and 10, it can be said that the higher the thickness, the higher the average growth of the liquid fraction.

Fig. 11 shows the melting maps of PCM (the temperature distribution along the fin length) for the different cases of sinusoidal fins. The results are reported at 2 different times during the melting process. With natural convection, extended surfaces also conduct heat to the outside, resulting in a temperature just below that of molten PCM. In this figure, small circulation cells between fins can be seen in molten regions. The circulation extends to a large portion of the enclosure by the advancement of melting, and a single central circulation occurs. The solid zones quickly disappear at the top of the enclosure due to the circulation flows and long fins at the top. The only un-melted region at 1800 s is at the bottom of the enclosure. This region slowly melts down as time passes.

By decreasing the H/L ratio 0.75 to 0.125, Within the enclosure, heat propagates identically. Fig. 11 shows a more uniform temperature distribution because of natural convection flow.

Finally, in order to better understand and compare the influence of all geometric parameters, a comprehensive and simultaneous comparison between all geometric parameters affecting the liquid fraction is accomplished in Fig. 12. This figure reveals that the lower the H/L ratio and the greater the thickness, a higher performance is achieved. But in the cases of 8 and 9, it can be seen that the case with a lower thickness has a higher liquid fraction, this is due to the fact that the effect of thickness on the liquid fraction is decreased as the time passes, because the amount of area related to PCM is much less than the rest of the parameters.

Figs. 13 and 14 illustrate velocity streamlines and vectors (as examples for case 2). An unfinned system has a shorter initial span than a finned system due to the dominance of convection flow. The velocity magnitudes of finned PCM systems are more stable throughout the working cycle. It is only the convection flow that determines the magnitude of the velocity during the melting of PCM. Using finned PCMs, The PCM continually transfers heat to the outside, resulting in a more constant natural convection flow. A more steady and continuous magnitude of velocity develops once the PCM has entirely melted. The magnitude of velocity rises with the number of stretched surfaces. Compared to more inclined PCM systems, the number of fins has a

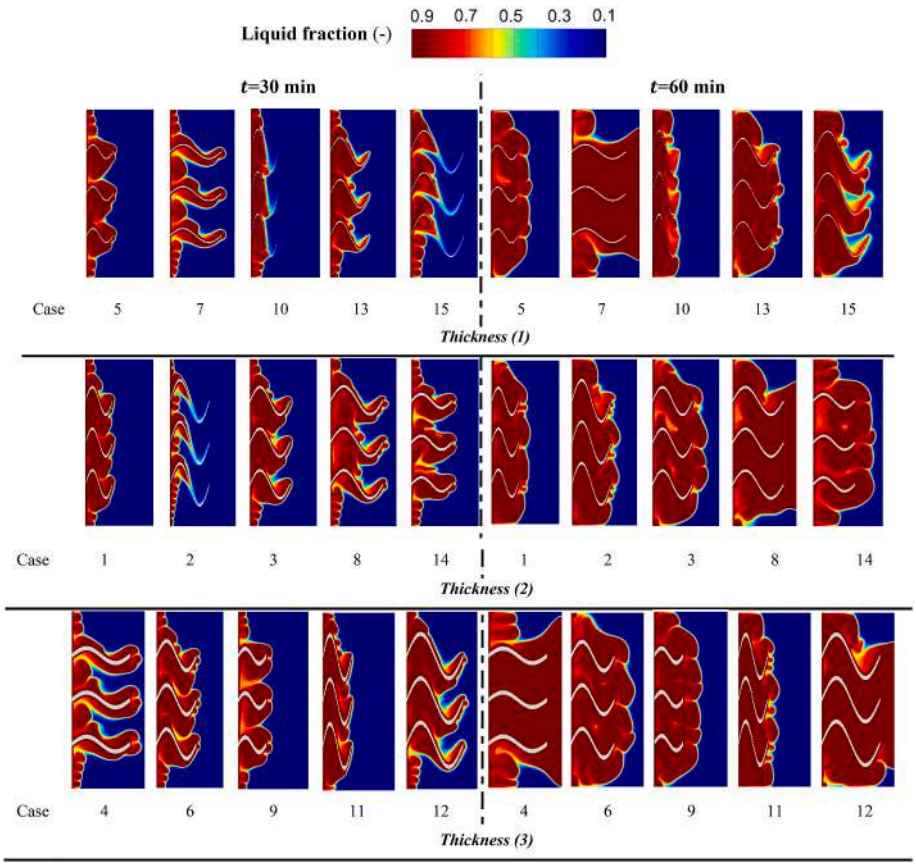

Fig. 10. Contour plot of liquid fraction for different defined cases at t = 30,60 min.

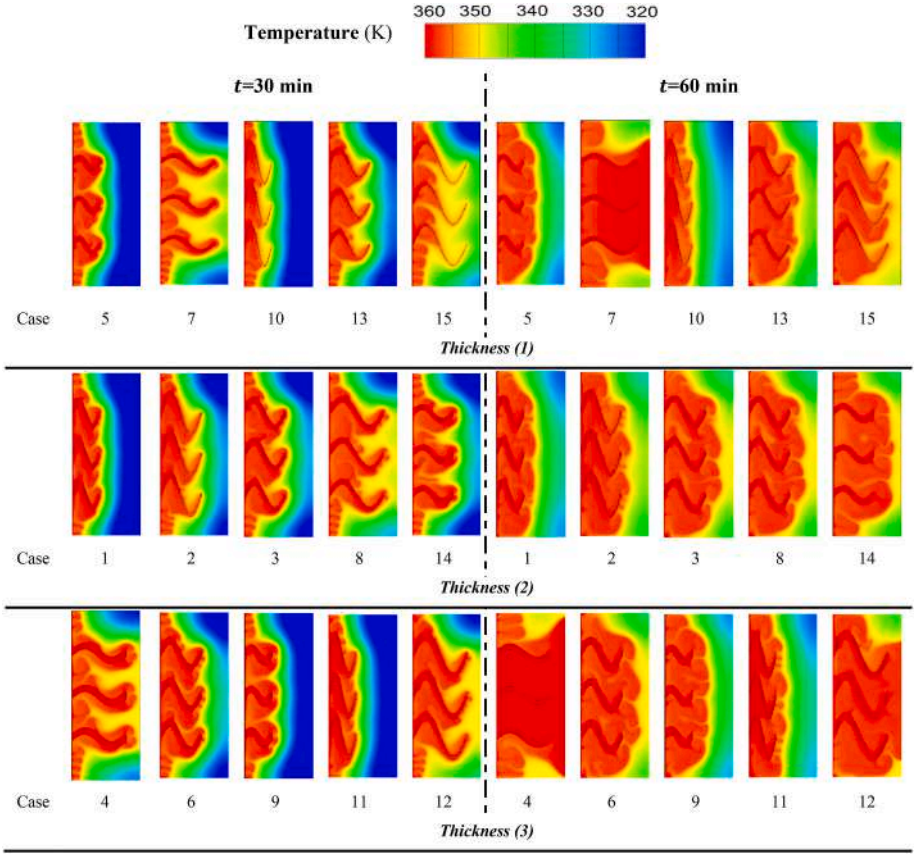

Fig. 11. Contour plot of temperature for different defined cases at t = 30,60 min.

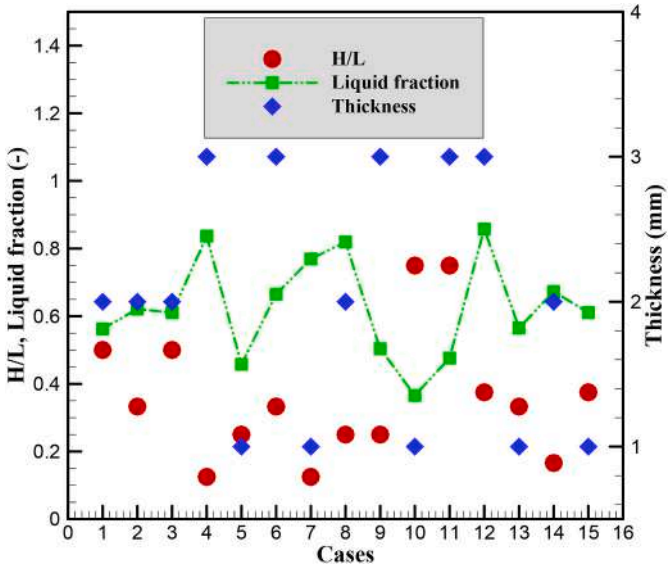

Fig. 12. The effect of all the geometrical parameters on the liquid fraction (at time-step of $t = 3600$ s).

considerable effect at low inclination degrees. The magnitude of velocity is also increased by reducing PCM thickness. By increasing the inclination angle, convection flow becomes more stable and uniform, resulting in more stable velocity magnitudes. During high inclination angles, the magnitude of velocity fluctuates more than during low inclination angles. The buoyancy-driven movement of liquid PCM may also be seen by keeping an eye on the molten PCM's velocity magnitude streamlines. When the melt front proceeds towards the extended surfaces, velocity vortices start to form close to the base. At first, the velocity magnitude is along the heater plate. The solid-liquid interface of PCM exhibits strong movement, resulting in increased convection currents and improved heat transfer rates in systems with extended surfaces.

Variation of mean heat transfer coefficient, heat transfer, and fin's temperature for different investigated cases is illustrated in Fig. 15. The figure expresses the rate of heat transfer between a solid surface and the surrounding fluid. The highest and lowest heat transfer coefficients are respectively obtained by cases of 9 and 10; because in case 9 the temperature difference between the wall and the temperature of the fluid block has its least value while is maximum in case 9. Another finding from this figure is that the fins' dimensions have a significant influence on the final studied time temperature. For example, large thickness and long length of case 4 has caused it to create a higher temperature due to more contact with the fluid.

It is evident in Fig. 14 that certain recirculation zones should be created, especially close to the fin walls, results in a greater degree of recirculation and, as a consequence, more heat transfer. Recirculation zones in storage energy systems enable some of the energy to be transmitted to the solid-liquid interface, leading to a quicker and more effective melting process. We can infer that these recirculation zones are more potent at longer melting durations (t = 3600 s). Due to greater recirculation zones surrounding heated surfaces, the rate of heat transfer will eventually rise. The cold and frozen region above the molten material interacts with the melting PCM to stop heat from naturally ascending, preventing heat from moving upstream. As a result, a vortex flow develops on the fins, enhancing the current's mixing with the fan wall and PCM.

The value of DhL (delta normalized[1] heat transfer coefficient)[2] and

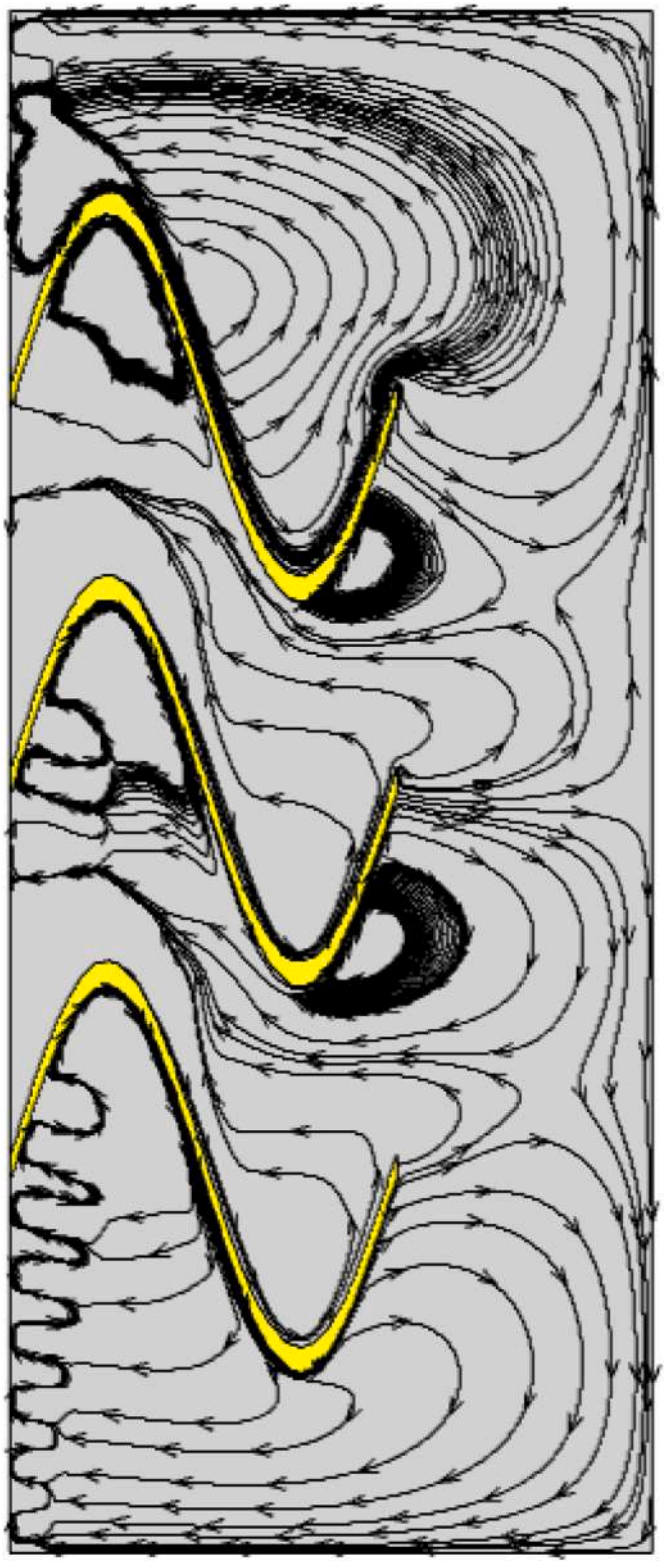

Fig. 13. Velocity streamlines for case 2.

Ste_{mom} (momentary Stefan number) parameters for different defined cases is illustrated as a radar chart in Fig. 16. Based on the definition of DhL, this graph is a comparison between liquid fraction and average heat transfer, and both of these are first normalized, meaning that both numbers are between 0 and 1. Based on this figure, the difference of normalized heat transfer coefficient and liquid fraction is maximized and minimized in the cases of 4 and 9, respectively. This means that case

[1] The normalized parameter is based on dividing the parameter to its maximum value: *Normalized parameter = Parameter/Maximum value*.

[2] DhL: Delta Normalized heat transfer Coefficient, liquid fraction, DhL = (Normalized heat transfer coefficient)-(Liquid fraction).

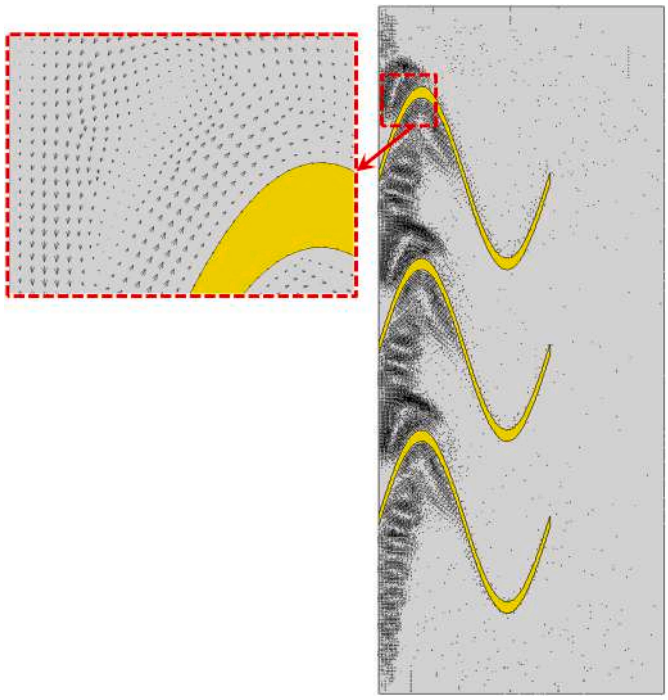

Fig. 14. Velocity vectors for case 2.

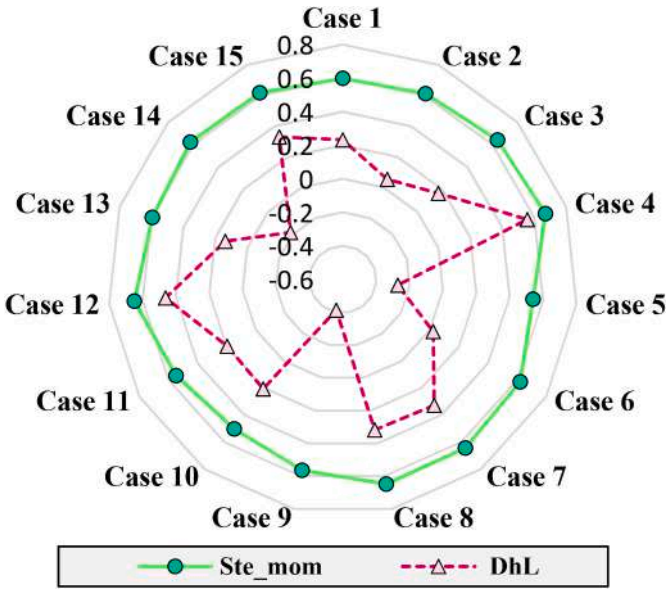

Fig. 16. Delta normalized heat transfer coefficient Liquid fraction and momentary Stefan number at time-step of $t = 3600$ s for different defined cases.

9 has higher normalized heat transfer coefficient than liquid fraction, which is not appropriate condition. For this, case 4 is selected as the best one because the value of liquid fraction is higher than normalized heat transfer coefficient in this case.

As another finding of this figure, the effect of geometric area can be discussed. For example, if cases 12 and 4 (which have different heights with same length and thickness) are compared, the negative effect of height in case 12 is understandable, which indicates that it does not have a good efficiency in proportion to the geometric area. The same trend can be analyzed in the comparison between cases 5 and 9. So this shows that in order to choose the right dimensions to create the best mode with a high efficiency, the area should be considered as a very important factor.

As it can be seen in Fig. 16, due to the higher amount of Ste_{mom} number in case 4 compared to other cases, this case is also selected as the best one based on this index. But the Ste_{mom} number cannot show the proper geometric shape of the fins, while the DhL number did it well. This figure shows that Ste_{mom} can only show well the effect of temperature difference on liquid fraction and does not consider all parameters.

Fig. 17 gives information about variation of Ste number during time for different defined cases. Increased momentary Ste number results from higher surface temperature. As it can be inferred from Figs. 16 and 17, PCM melting rates were influenced by the momentary temperature difference between surface and momentary temperature; as the momentary temperature difference increased, the liquid fraction increased more rapidly, and the melting rate decreased.

The remaining part of the results is specified to present the outputs of entropy generation analysis. As a thermodynamic characteristic, the entropy generation combines fluid flow and heat transfer principles. So that, it is composed of two terms: thermal and frictional. Different terms of entropy generation is presented in Fig. 18. Due to the nature of the studied working fluid, thermal entropy generation itself comprises of two solid + fluid parts. Since there are no velocity gradients in the solid part, friction only produces entropy in the fluid part. Based on this figure, the values of frictional term is very low and can be ignored from total entropy generation ($\dot{S}_{g,h} \gg \dot{S}_{g,f}$). Furthermore in thermal term, the order-of-magnitude of fluid part is higher than that of for solid part.

Finally, to demonstrate high efficiency of the proposed sinusoidal fins for using in LHTES systems, the outputs of the problem are compared with straight fins (distribution of the liquid fraction and temperature for straight fins with length of 20 mm and thickness of 2 mm is presented in Fig. A1 in Appendix A; also, variation of these two parameters is depicted in Fig. A2). Fig. 19 illustrates the percentage of

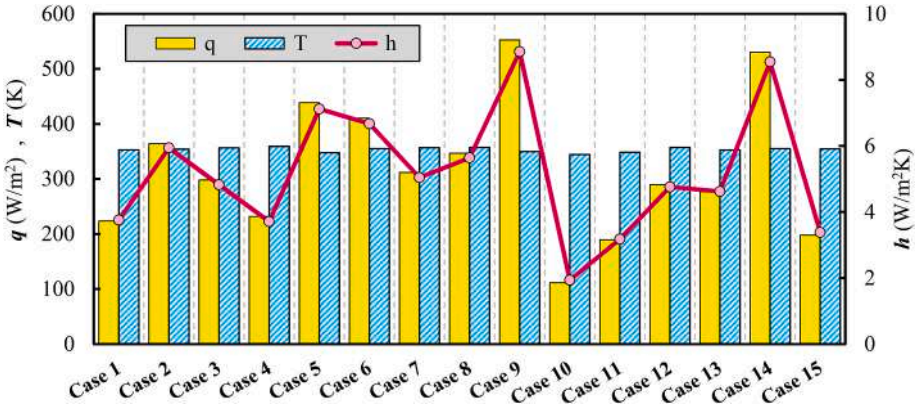

Fig. 15. Heat transfer rate and coefficient and temperature at time-step of $t = 3600$ s for different defined cases.

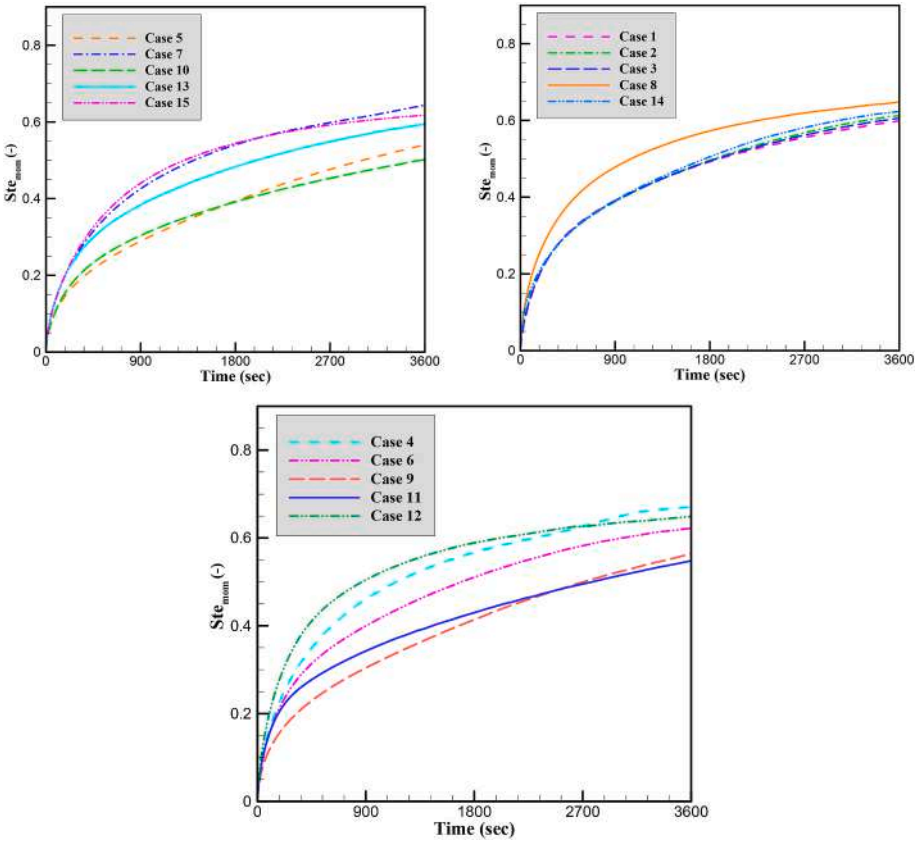

Fig. 17. Variation of the momentary Stefan number versus time for different defined cases.

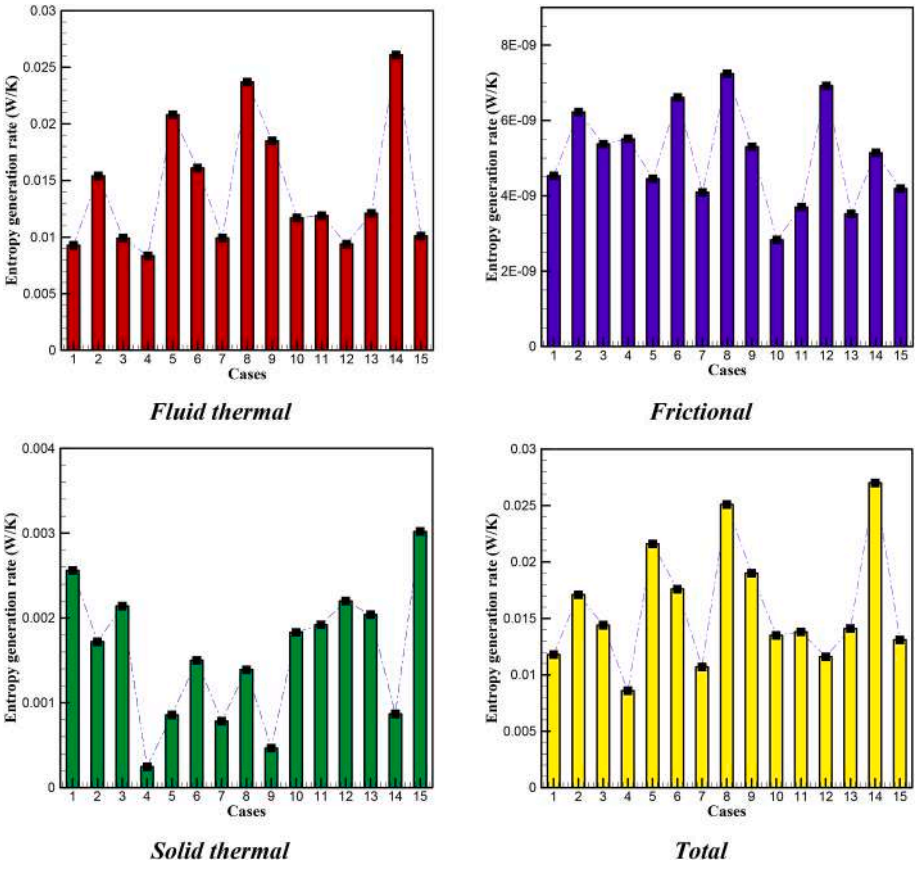

Fig. 18. Comparison fluid thermal, solid thermal, frictional, and total entropy generation terms for different defined cases.

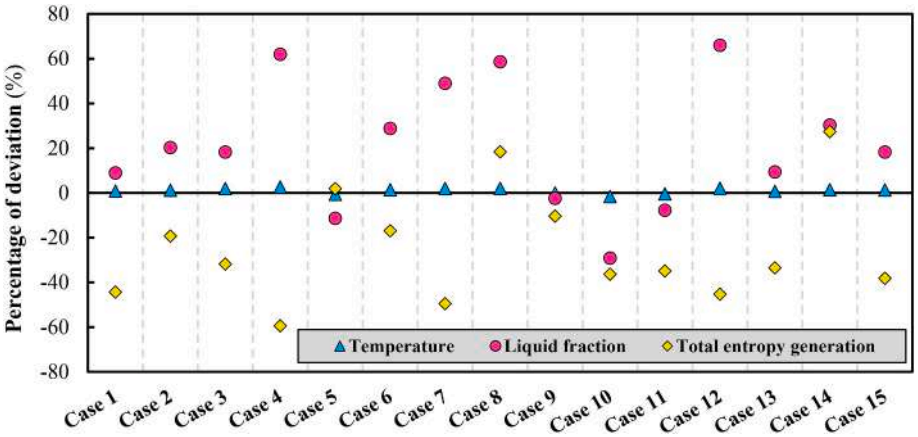

Fig. 19. Comparison of the thermo-hydraulic characteristics of sinusoidal and straight fins for using in LHTES systems.

deviation between sinusoidal and straight fins.[3] As it can be inferred from this figure, in most of the cases, the sinusoidal fins shows higher liquid fraction and lower entropy generation. This proves superiority of sinusoidal fins over straights and hence this proposal is efficient from both of the heat transfer and thermodynamics stand-points.

6. Conclusion

The melting rate of RT82 as a PCM was quantitatively examined to see how internal sinusoidal fins may improve heat transmission for a heat sink. Different design and operation parameters including the fins' length (L), height (H), and thickness (b) were investigated on the heat transfer and entropy generation characteristics. A robust validated CFD simulation was developed as an unsteady laminar flow. A comprehensive sensitivity analysis was also conducted to assess the effects of geometrical parameters (by defining 15 different geometries) on various thermo-hydraulic and heat transfer indices. In summary, the main achievements of this paper can be concluded as following items:

- The simulation results reveal that geometrical parameters significantly affect the time for complete melting; fin thickness has a small effect on melting rate time compared to fin length and number.
- The second-law analysis demonstrated that the values of frictional entropy generation is very low and can be ignored from total entropy generation ($\dot{S}_{g,h} \gg \dot{S}_{g,f}$). Furthermore in thermal entropy generation, which is composed of two fluid and solid parts, the order-of-magnitude of fluid part is higher than that of for solid part.
- The case 4 ($L = 40$ mm, $H = 5$ mm, and $b = 3$ mm) achieved the complete melting earlier with respect to other cases. The highest growth of normalized liquid fraction compared to normalized heat transfer coefficient is achieved in case 4 which results in Dhl number of about 0.55. Also, the second-law analysis revealed that the lowest entropy is generated in this case.
- Comparing the results of optimal case (case 4) with the simple straight fins illustrated that the liquid fraction and entropy generation rate are respectively 62% higher and 59.5% lower in case 4.
- This paper proposed a comprehensive framwork around thermo-hydraullic improvement of simultaneous usage of PCM and internal fins in LHTESs. As suggestion for future works, the effect of porous media on the surface of the fins can be assessed on the heat transfer coefficient and liquid fraction. Another suggestion is to investigated nano-particles utilization effect on liquid fraction.

CRediT authorship contribution statement

Ali Tavakoli: Writing – original draft, Writing – review & editing, Visualization, Methodology, Investigation, Validation, Software. **Mahmood Farzaneh-Gord:** Supervision, Project administration, Formal analysis, Methodology, Visualization, Writing – review & editing. **Amir Ebrahimi-Moghadam:** Visualization, Formal analysis, Writing – review & editing.

Declaration of competing interest

The authors declare that they have no known competing financial interests or personal relationships that could have appeared to influence the work reported in this paper

Data availability

Data will be made available on request.

Abbreviations

Cu	copper
Ti	titanium
$\dot{S}$	entropy generation (EG) rate (W/K)
c_P	specific heat capacity
c_{Pw}	specific heat capacity of water
d	coil diameter (m)
d_f	diameters of base fluid particle (m)
h	average convective heat transfer coefficient (W/(m^2. K))

[3] Percentage of deviation $= \frac{\text{sinusoidal fin} - \text{straight fin}}{\text{straight fin}} \times 100$

k	thermal conductivity
Nu	Nusselt number
P	pressure (Pa)
T	temperature (K)
T_0	reference temperature, 273 K
r	radial distance (m)
u	x-velocity (m/s)
μ	dynamic viscosity (Pa.s)
$\mathrm{Ste}_{\mathrm{mom}}$	momentary Stefan number (−)
DhL	delta normalized heat transfer coefficient liquid fraction (−)
PCM	phase change material
C_p	specific heat (J/kg.K)
HTF	heat transfer fluid
T_{mom}	momentary time (s)
TES	thermal energy storage
A_{mush}	mushy zone constant
g	acceleration due to gravity (m/s^2)
t	time (s)
v	velocity (m/s)
CTE	coefficient of thermal expansion
h_e	Enthalpy

Greek symbol

ρ	density (kg/m^3)
μ	dynamic discosity (Pa.s)
φ	volume fraction
β	coefficient of thermal expansion (1/K)
Γ	latent heat of fusion (kJ/kg)
κ	constant of Boltzmann, 1.381×10^{-23} J/K
λ	liquid fraction
ε	small value

Subscripts

f	liquid phase
s	solid phase
I	liquid phase
ref	reference

Appendix A. Results of simple case with straight fins

In this section, the outputs of simulation for a simple case with straight fins is presented. The length and thickness of fins are 20 mm and 2 mm, respectively. Fig. A1 shows distribution of liquid fraction and temperature within the solution domain for a time-step of $t = 3600$ s. Also, variation of these two parameters over the time during the melting process is depicted in Fig. A2.

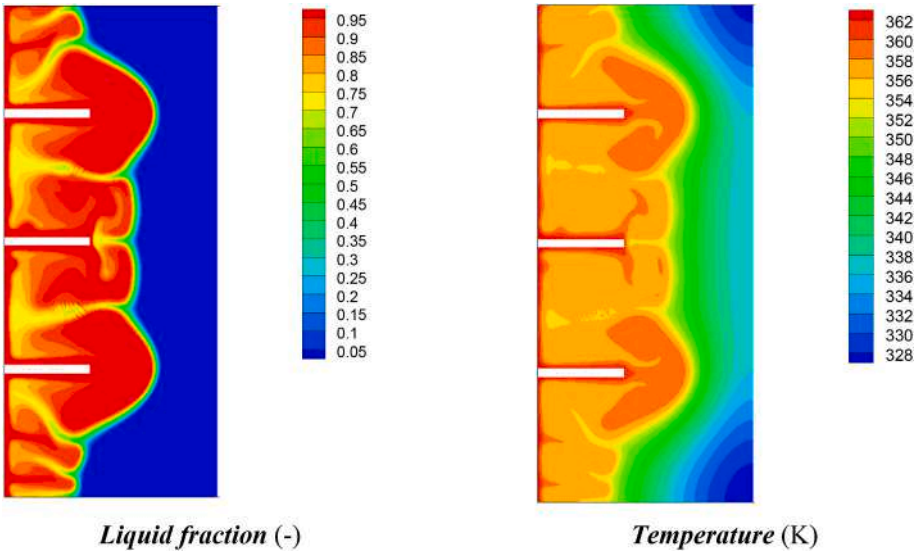

Fig. A1. Contour plot of liquid fraction and temperature for straight fin.

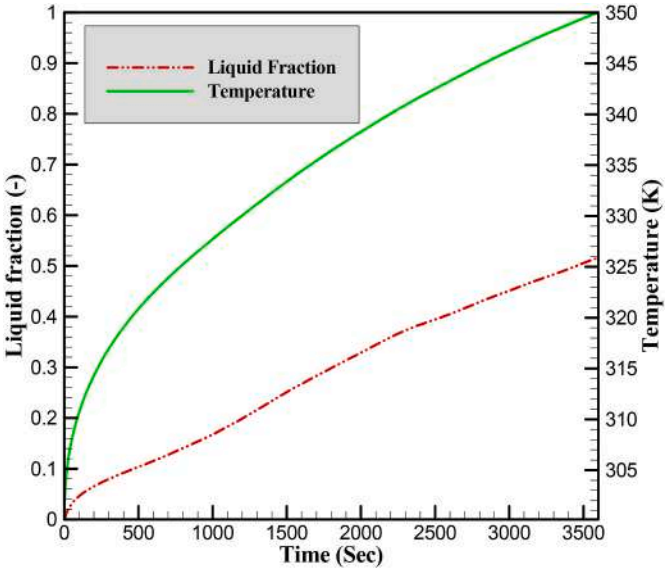

Fig. A2. Variation of the liquid fraction and temperature versus time for straight fin.

References

[1] A.M. Saeed, A. Abderrahmane, N.A.A. Qasem, A. Mourad, M. Alhazmi, S.E. Ahmed, K. Guedri, A numerical investigation of a heat transfer augmentation finned pear-shaped thermal energy storage system with nano-enhanced phase change materials, J. Energy Storage 53 (2022), 105172, https://doi.org/10.1016/j.est.2022.105172.

[2] Z. Dai, J. Xie, W. Liu, X. Wang, L. Zhang, Z. Zhou, J. Li, X. Ren, Effective strategy to achieve excellent energy storage properties in lead-free BaTiO3-based bulk ceramics, ACS Appl. Mater. Interfaces 12 (2020) 30289–30296, https://doi.org/10.1021/acsami.0c02832.

[3] X. Zhang, Y. Tang, F. Zhang, C.-S. Lee, A novel aluminum–graphite dual-ion battery, Adv. Energy Mater. 6 (2016), 1502588, https://doi.org/10.1002/aenm.201502588.

[4] M. Wang, C. Jiang, S. Zhang, X. Song, Y. Tang, H.-M. Cheng, Reversible calcium alloying enables a practical room-temperature rechargeable calcium-ion battery with a high discharge voltage, Nat. Chem. 10 (2018) 667–672, https://doi.org/10.1038/s41557-018-0045-4.

[5] S. Mu, Q. Liu, P. Kidkhunthod, X. Zhou, W. Wang, Y. Tang, Molecular grafting towards high-fraction active nanodots implanted in N-doped carbon for sodium dual-ion batteries, Natl. Sci. Rev. 8 (2021) 178, https://doi.org/10.1093/nsr/nwaa178.

[6] X. Feng, L. Jiang, D. Li, S. Tian, X. Zhu, H. Wang, C. He, K. Li, Progress and key challenges in catalytic combustion of lean methane, J. Energy Chem. 75 (2022) 173–215, https://doi.org/10.1016/j.jechem.2022.08.001.

[7] W. Cui, T. Si, X. Li, X. Li, L. Lu, T. Ma, Q. Wang, Heat transfer analysis of phase change material composited with metal foam-fin hybrid structure in inclination container by numerical simulation and artificial neural network, Energy Rep. 8 (2022) 10203–10218, https://doi.org/10.1016/j.egyr.2022.07.178.

[8] N.H. Abu-Hamdeh, K.A. Alnefaie, Assessment of thermal performance of PCM in latent heat storage system for different applications, Sol. Energy 177 (2019) 317–323, https://doi.org/10.1016/j.solener.2018.11.035.

[9] Y. Zhang, Z.-X. Chi, K.-Q. Li, Fuzzy multi-class classifier based on support vector data description and improved PCM, Expert Syst. Appl. 36 (2009) 8714–8718, https://doi.org/10.1016/j.eswa.2008.03.026.

[10] H. Chang, Z. Han, X. Li, T. Ma, Q. Wang, Experimental investigation on heat transfer performance based on average thermal-resistance ratio for supercritical carbon dioxide in asymmetric airfoil-fin printed circuit heat exchanger, Energy 254 (2022), 124164, https://doi.org/10.1016/j.energy.2022.124164.

[11] D. Liu, K. Xie, H. Zhang, Y. Qiang, D. Yang, Z. Wang, L. Zhu, N. Akkurt, Y. Du, M. Shen, L. Zhong, F. Yu, Q. Xu, Numerical evaluation of convective heat transfer properties of two-dimensional rotating PCM melt in the unilaterally heated rectangular container, Renew. Energy 193 (2022) 920–940, https://doi.org/10.1016/j.renene.2022.05.009.

[12] B. Buonomo, O. Manca, S. Nardini, R.E. Plomitallo, Numerical study on latent heat thermal energy storage system with PCM partially filled with aluminum foam in local thermal equilibrium, Renew. Energy 195 (2022) 1368–1380, https://doi.org/10.1016/j.renene.2022.06.122.

[13] A.R. Abdulmunem, P. Mohd Samin, H. Abdul Rahman, H.A. Hussien, I. Izmi Mazali, H. Ghazali, Numerical and experimental analysis of the tilt angle's effects on the characteristics of the melting process of PCM-based as PV cell's backside heat sink, Renew. Energy 173 (2021) 520–530, https://doi.org/10.1016/j.renene.2021.04.014.

[14] A. Pizzolato, A. Sharma, K. Maute, A. Sciacovelli, V. Verda, Design of effective fins for fast PCM melting and solidification in shell-and-tube latent heat thermal energy storage through topology optimization, Appl. Energy 208 (2017) 210–227, https://doi.org/10.1016/j.apenergy.2017.10.050.

[15] M. Sheikholeslami, Numerical simulation for solidification in a LHTESS by means of nano-enhanced PCM, J. Taiwan Inst. Chem. Eng. 86 (2018) 25–41, https://doi.org/10.1016/j.jtice.2018.03.013.

[16] O.K. Yagci, M. Avci, O. Aydin, Melting and solidification of PCM in a tube-in-shell unit: effect of fin edge lengths' ratio, J. Energy Storage 24 (2019), 100802, https://doi.org/10.1016/j.est.2019.100802.

[17] R. Dai, J. Mostaghimi, N. Li, T. Deng, Q. Wang, M. Zeng, Charging time and energy storage rate analysis of fin effect inside the horizontal tube for thermal energy storage, J. Clean. Prod. 273 (2020), 123030, https://doi.org/10.1016/j.jclepro.2020.123030.

[18] M. Gürtürk, B. Kok, A new approach in the design of heat transfer fin for melting and solidification of PCM, Int. J. Heat Mass Tran. 153 (2020), 119671, https://doi.org/10.1016/j.ijheatmasstransfer.2020.119671.

[19] B. Kok, Examining effects of special heat transfer fins designed for the melting process of PCM and Nano-PCM, Appl. Therm. Eng. 170 (2020), 114989, https://doi.org/10.1016/j.applthermaleng.2020.114989.

[20] T. Pirasaci, Investigation of phase state and heat storage form of the phase change material (PCM) layer integrated into the exterior walls of the residential-apartment during heating season, Energy 207 (2020), 118176, https://doi.org/10.1016/j.energy.2020.118176.

[21] M. Arıcı, E. Tütüncü, C. Yıldız, D. Li, Enhancement of PCM melting rate via internal fin and nanoparticles, Int. J. Heat Mass Tran. 156 (2020), 119845, https://doi.org/10.1016/j.ijheatmasstransfer.2020.119845.

[22] Y. Yang, W. Wu, S. Fu, H. Zhang, Study of a novel ceramsite-based shape-stabilized composite phase change material (PCM) for energy conservation in buildings, Construct. Build. Mater. 246 (2020), 118479, https://doi.org/10.1016/j.conbuildmat.2020.118479.

[23] F. Li, N. Muhammad, E. Abohamzeh, A.K.A. Hakeem, M.R. Hajizadeh, Z. Li, Q.-V. Bach, Finned unit solidification with use of nanoparticles improved PCM, J. Mol. Liq. 314 (2020), 113659, https://doi.org/10.1016/j.molliq.2020.113659.

[24] C. Zhao, M. Opolot, M. Liu, F. Bruno, S. Mancin, K. Hooman, Numerical study of melting performance enhancement for PCM in an annular enclosure with internal-external fins and metal foams, Int. J. Heat Mass Tran. 150 (2020), 119348, https://doi.org/10.1016/j.ijheatmasstransfer.2020.119348.

[25] F.S. dos Santos, K.A.R. Ismail, F.A.M. Lino, A. Arabkoohsar, T.G.S. Lago, Parametric investigation of the enhancing effects of finned tubes on the solidification of PCM, Int. J. Heat Mass Tran. 152 (2020), 119485, https://doi.org/10.1016/j.ijheatmasstransfer.2020.119485.

[26] M. Taghilou, E. Khavasi, Thermal behavior of a PCM filled heat sink: the contrast between ambient heat convection and heat thermal storage, Appl. Therm. Eng. 174 (2020), 115273, https://doi.org/10.1016/j.applthermaleng.2020.115273.

[27] T. Xu, S.N. Gunasekara, J.N. Chiu, B. Palm, S. Sawalha, Thermal behavior of a sodium acetate trihydrate-based PCM: T-history and full-scale tests, Appl. Energy 261 (2020), 114432, https://doi.org/10.1016/j.apenergy.2019.114432.

[28] M.E. Nakhchi, M. Hatami, M. Rahmati, A numerical study on the effects of nanoparticles and stair fins on performance improvement of phase change thermal

energy storages, Energy 215 (2021), 119112, https://doi.org/10.1016/j.energy.2020.119112.
[29] H. Soltani, M. Soltani, H. Karimi, J. Nathwani, Optimization of shell and tube thermal energy storage unit based on the effects of adding fins, nanoparticles and rotational mechanism, J. Clean. Prod. 331 (2022), 129922, https://doi.org/10.1016/j.jclepro.2021.129922.
[30] Z.-J. Zheng, X. Cai, C. Yang, Y. Xu, Improving the solidification performance of a latent heat thermal energy storage unit using arrow-shaped fins obtained by an innovative fast optimization algorithm, Renew. Energy 195 (2022) 566–577, https://doi.org/10.1016/j.renene.2022.06.031.
[31] J. Li, Z.R. Abdulghani, M.N. Alghamdi, K. Sharma, H. Niyas, H. Moria, A. Arsalanloo, Effect of twisted fins on the melting performance of PCM in a latent heat thermal energy storage system in vertical and horizontal orientations: energy and exergy analysis, Appl. Therm. Eng. (2022), 119489, https://doi.org/10.1016/j.applthermaleng.2022.119489.
[32] M.S. Yousef, H. Hassan, Energy payback time, exergoeconomic and enviroeconomic analyses of using thermal energy storage system with a solar desalination system: an experimental study, J. Clean. Prod. 270 (2020), 122082, https://doi.org/10.1016/j.jclepro.2020.122082.
[33] M. Palacio, A. Rincon, M. Carmona, Experimental comparative analysis of a flat plate solar collector with and without PCM, Sol. Energy 206 (2020) 708–721, https://doi.org/10.1016/j.solener.2020.06.047.
[34] V.S. Vigneswaran, G. Kumaresan, B.V. Dinakar, K.K. Kamal, R. Velraj, Augmenting the productivity of solar still using multiple PCMs as heat energy storage, J. Energy Storage 26 (2019), 101019, https://doi.org/10.1016/j.est.2019.101019.
[35] M.S. Mahdi, H.B. Mahood, J.M. Mahdi, A.A. Khadom, A.N. Campbell, Improved PCM melting in a thermal energy storage system of double-pipe helical-coil tube, Energy Convers. Manag. 203 (2020), 112238, https://doi.org/10.1016/j.enconman.2019.112238.
[36] T. Sathe, A.S. Dhoble, Thermal analysis of an inclined heat sink with finned PCM container for solar applications, Int. J. Heat Mass Tran. 144 (2019), 118679, https://doi.org/10.1016/j.ijheatmasstransfer.2019.118679.
[37] I. Sarani, S. Payan, S.A. Nada, A. Payan, Numerical investigation of an innovative discontinuous distribution of fins for solidification rate enhancement in PCM with and without nanoparticles, Appl. Therm. Eng. 176 (2020), 115017, https://doi.org/10.1016/j.applthermaleng.2020.115017.
[38] M.E. Nakhchi, J.A. Esfahani, Improving the melting performance of PCM thermal energy storage with novel stepped fins, J. Energy Storage 30 (2020), 101424, https://doi.org/10.1016/j.est.2020.101424.
[39] S. Duan, L. Wang, Z. Zhao, C. Zhang, Experimental study on thermal performance of an integrated PCM Trombe wall, Renew. Energy 163 (2021) 1932–1941, https://doi.org/10.1016/j.renene.2020.10.081.
[40] A.E. Kabeel, M.A. Teamah, M. Abdelgaied, G.B. Abdel Aziz, Modified pyramid solar still with v-corrugated absorber plate and PCM as a thermal storage medium, J. Clean. Prod. 161 (2017) 881–887, https://doi.org/10.1016/j.jclepro.2017.05.195.
[41] Y. Hou, H. Chen, X. Liu, Experimental study on the effect of partial filling of copper foam on heat storage of paraffin-based PCM, Renew. Energy 192 (2022) 561–571, https://doi.org/10.1016/j.renene.2022.04.084.
[42] L. Pu, S. Zhang, L. Xu, Z. Ma, X. Wang, Numerical study on the performance of shell-and-tube thermal energy storage using multiple PCMs and gradient copper foam, Renew. Energy 174 (2021) 573–589, https://doi.org/10.1016/j.renene.2021.04.061.
[43] F. Selimefendigil, H.F. Öztop, N. Abu-Hamdeh, Optimization of phase change process in a sinusoidal-wavy conductive walled cylinder with encapsulated-phase change material during magnetohydrodynamic nanofluid convection, J. Energy Storage 55 (2022), 105512, https://doi.org/10.1016/j.est.2022.105512.
[44] E. Douvi, C. Pagkalos, G. Dogkas, M.K. Koukou, V.N. Stathopoulos, Y. Caouris, M. G. Vrachopoulos, Phase change materials in solar domestic hot water systems: a review, Int. J. Thermofluids. 10 (2021), 100075, https://doi.org/10.1016/j.ijft.2021.100075.
[45] A. Ebrahimi-Moghadam, A.J. Moghadam, Optimal design of geometrical parameters and flow characteristics for Al2O3/water nanofluid inside corrugated heat exchangers by using entropy generation minimization and genetic algorithm methods, Appl. Therm. Eng. 149 (2019) 889–898, https://doi.org/10.1016/j.applthermaleng.2018.12.068.
[46] A.A. Al-Abidi, S. Mat, K. Sopian, M.Y. Sulaiman, A.T. Mohammad, Internal and external fin heat transfer enhancement technique for latent heat thermal energy storage in triplex tube heat exchangers, Appl. Therm. Eng. 53 (2013) 147–156, https://doi.org/10.1016/j.applthermaleng.2013.01.011.
[47] L.-E. Yan, N.H. Abu-Hamdeh, R.A.R. Bantan, M.M. Selim, Heat storage unit for melting of paraffin considering hybrid nanomaterial and helical tubes, J. Energy Storage 44 (2021), 103427, https://doi.org/10.1016/j.est.2021.103427.
[48] A. Shahsavar, A. Shaham, C. Yildiz, M. Arici, Entropy generation characteristics of phase change material in a variable wavy walled triplex tube latent heat storage unit for battery thermal management system, J. Energy Storage 51 (2022), 104374, https://doi.org/10.1016/j.est.2022.104374.
[49] S. Entezari, A. Taheri, M. Khatibi, H. Niazmand, Acceleration of melting process of phase change material using an innovative triplex-tube helical-coil storage unit: three-dimensional numerical study, J. Energy Storage 39 (2021), 102603, https://doi.org/10.1016/j.est.2021.102603.
[50] A. Ebrahimi-Moghadam, B. Mohseni-Gharyehsafa, M. Farzaneh-Gord, Using artificial neural network and quadratic algorithm for minimizing entropy generation of Al2O3-EG/W nanofluid flow inside parabolic trough solar collector, Renew. Energy 129 (2018) 473–485, https://doi.org/10.1016/j.renene.2018.06.023.
[51] D. Xiao, Y. Hu, Y. Wang, H. Deng, J. Zhang, B. Tang, J. Xi, S. Tang, G. Li, Wellbore cooling and heat energy utilization method for deep shale gas horizontal well drilling, Appl. Therm. Eng. 213 (2022), 118684, https://doi.org/10.1016/j.applthermaleng.2022.118684.
[52] A. Ebrahimi-Moghadam, F. Gohari, D. Hoseinzade, M. Deymi-Dashtebayaz, A comprehensive thermo-hydraulic analysis and optimization of turbulent TiO2/W-EG nano-fluid flow inside double-pipe heat exchangers with helical coil inserts, J. Brazilian Soc. Mech. Sci. Eng. 42 (2020) 232, https://doi.org/10.1007/s40430-020-02320-7.
[53] R. Dormohammadi, M. Farzaneh-Gord, A. Ebrahimi-Moghadam, M.H. Ahmadi, Heat transfer and entropy generation of the nanofluid flow inside sinusoidal wavy channels, J. Mol. Liq. 269 (2018) 229–240, https://doi.org/10.1016/j.molliq.2018.07.119.
[54] A. Ebrahimi-Moghadam, S. Kowsari, F. Farhadi, M. Deymi-Dashtebayaz, Thermohydraulic sensitivity analysis and multi-objective optimization of Fe3O4/H2O nanofluid flow inside U-bend heat exchangers with longitudinal strip inserts, Appl. Therm. Eng. 164 (2020), 114518, https://doi.org/10.1016/j.applthermaleng.2019.114518.
[55] J. Sodagar-Abardeh, A. Ebrahimi-Moghadam, M. Farzaneh-Gord, A. Norouzi, Optimizing chevron plate heat exchangers based on the second law of thermodynamics and genetic algorithm, J. Therm. Anal. Calorim. 139 (2020) 3563–3576, https://doi.org/10.1007/s10973-019-08742-3.